Determining the Optimal Parameters in a Distant Radar NDE Technique for Debonding Detection of GFRP-concrete Systems

Tzu-Yang Yu

Department of Civil and Environmental Engineering,
University of Massachusetts Lowell
FA107B, One University Avenue, Lowell, MA 01854, U.S.A.

ABSTRACT

In the distant detection of debonding in glass fiber reinforced polymer (GFRP)-retrofitted concrete systems using radar NDE techniques, revealing the presence of debonding in reconstructed images is essential to the success of the techniques. An optimization scheme based on mathematical morphology is proposed for determining the optimal measurement and processing parameters in a distant radar NDE technique for debonding detection. Inverse synthetic aperture radar (ISAR) and backprojection algorithms are applied in the technique. Measurement (incident frequency and angle) and processing (frequency bandwidth and angular range) parameters are defined in this work. Performance of the optimization scheme is validated by laboratory ISAR measurements on GFRP-retrofitted concrete cylinders using radar signals in 8∼18 GHz. From the results it is shown that better detection can be achieved by optimized measurements and processing.

Keywords: Radar NDE, distant inspection, GFRP-concrete cylinders, backprojection algorithms, mathematical morphology

1. INTRODUCTION

Deterioration of civil infrastructure systems is an inevitable result of a loading process in which the systems experience physical and chemical attacks at various frequencies, durations, and intensities. Civil infrastructure systems degrade due to high-frequency, low-intensity attacks (e.g., service loading), as well as due to low-frequency, high-intensity attacks (e.g., earthquakes), during their service life. Consequently, their structural integrity (or capacity, health) is degraded and, in most cases, remains undetermined. In the 2009 ASCE (American Society of Civil Engineers) Report Card for Americas Infrastructure, the U.S. infrastructure receives an overall grade of D, indicating that America has an infrastructure that is poorly maintained, unable to meet current and future demands, and in some cases, unsafe and suggesting a total cost of $2.2 trillion for repair [ASCE (2009)]. It can be envisioned that repairing degraded civil infrastructure will demand the development of advanced rehabilitation, inspection, and monitoring technologies to achieve efficient infrastructure maintenance and management in the U.S., especially in a financially difficult time.

A distant radar NDE technique termed FAR (far-field airborne radar) NDT (nondestructive testing) has been proposed for the non-contact inspection of near-surface delamination and defects in multi-layer systems like GFRP (glass fiber reinforced polymer)-wrapped concrete columns[1,2]. The proposed technique aims at providing a distant inspection capability that can reveal the in-depth condition of multi-layer systems using electromagnetic waves at the gigahertz (GHz) frequency range (e.g., 8∼18 GHz). Laboratory inverse synthetic aperture radar (ISAR) measurements on GFRP-concrete cylinders were collected at the Massachusetts Institute of Technology Lincoln Laboratory (MIT LL) to physically validate the feasibility of FAR NDT. In the FAR NDT technique, the presence of near-surface defects (e.g., debonding and delaminations) is revealed in reconstructed images enabled by the backprojection algorithms.

Further author information: (Send correspondence to T.-Y. Yu)
E-mail: tzuyang_yu@UML.EDU, Telephone: 1 617 230 7402

Nondestructive Characterization for Composite Materials, Aerospace Engineering, Civil Infrastructure, and Homeland Security 2009, edited by H. Felix Wu, Aaron A. Diaz, Peter J. Shull, Dietmar W. Vogel,
Proc. of SPIE Vol. 7294, 72940S · © 2009 SPIE · CCC code: 0277-786X/09/$18 · doi: 10.1117/12.815895

The objective of this paper is to investigate the performance of FAR NDT technique by studying the optimal combination of measurement (incident frequency and angle) and processing (frequency bandwidth and angular range) parameters defined in the technique. In this paper, methodology of the signal processing and image reconstruction in FAR NDT is briefly explained. Damage detectability in reconstructed images is quantitatively evaluated using an index (Euler's number) defined in mathematical morphology. Optimal measurement and processing parameters are determined by achieving maximum detection in the reconstructed images.

In what follows, methodology of signal processing and image reconstruction is provided.

2. METHODOLOGY

2.1 Signal Processing and Image Reconstruction

In the ISAR measurements of FAR NDT, monostatic radar operation is applied. The radar operation at different incident angles (θ_m) and frequencies (ω_n) forms a data plane as illustrated in Figure 1. The time-dependent scattering response of a point scatterer $\bar{r}_j$ observed by the radar at $\bar{r}_s$ is[3]

$$S(\bar{r}_{s,j}, t) = \frac{1}{R_{s,j}^2} \int_{\omega_c - \pi B}^{\omega_c + \pi B} d\omega \cdot \exp[i\omega t] \tag{1}$$

where $\bar{r}_{s,j} = \bar{r}_s - \bar{r}_j$, $\bar{r}_s$ is the radar position vector, $\bar{r}_j$ is the position vector of the j^{th} scatter, $R_{s,j} = |\bar{r}_{s,j}|$ is the distance between the radar and the j^{th}, ω_c is the radian center frequency, i is the imaginary number, ω is the radian frequency variable, B is the frequency bandwidth, and t is the time variable. Replacing the time t in $S(\bar{r}_s, t)$ with $\hat{t} = t - \dfrac{2R_s}{c}$ results in the range-compressed $S(\bar{r}_s, \hat{t})$.

$$S(\bar{r}_{s,j}, \hat{t}) = \frac{B}{R_{s,j}^2} \exp[i\omega\hat{t}] \cdot \mathrm{sinc}(B\hat{t}) \tag{2}$$

where $sinc\,(x) = \dfrac{\sin \pi x}{\pi x}$. The integration of $S(\bar{r}_{s,j}, \hat{t})$ in cylindrical coordinate systems (where the ISAR motion is convenient to define) yields

$$D(\xi, \hat{t}) = \int_0^{R_s} d\bar{r}_j \int_0^{2\pi} d\phi_j \cdot G(\bar{r}_j, \phi_j) S(\bar{r}_{s,j}, \hat{t}) \tag{3}$$

where $\xi = R_s\phi_i$, $G(\bar{r}_j, \phi_j)$ is the scattering amplitude density function at $(\bar{r}_j, \phi_j)$. The backprojection processing of $D(\xi, \hat{t})$ provides $B_{BP}(\xi, \hat{t})$, and the backprojection image image is obtained by

$$I(\bar{r}, \phi) = \int_0^{R_s\theta_{\mathrm{int}}} d\xi \cdot F(\xi, \hat{t}) \tag{4}$$

where $(\bar{r}, \phi)$ is defined on the range vs. cross-range plane where the in-depth profile of target structure can be described. Details of ISAR measurements can be found in the literature on radar imaging.[3,4] In the FAR NDT technique, backprojection algorithms are applied because they provide (1) lower and localized artifact levels than frequency-domain algorithms, (2) easy adjustment to an approximate inverse formula for perturbed problems, (3) convenient implementation for parallel computing with limited inter-processor communications, and (4) simple motion compensation by time-shift operation.[5,6] Computational advantages of the backprojection algorithms are due to the use of a matched filter to prevent potential data discontinuity from happening and to enhance computational efficiency by pre-processing the filter. In implementing the backprojection algorithms, the fast backprojection algorithm is adopted[7].

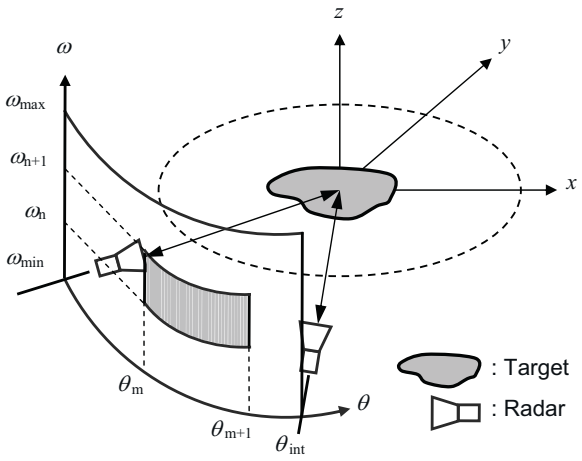

Figure 1. The data plane concept in the FAR NDT technique

2.2 Damage Detectability – Mathematical Morphology

In this work, the presence of near-surface damages is revealed by the reconstructed backprojection images and quantitatively evaluated by mathematical morphology. Features of the backprojection images are extracted by morphological operations (dilation and erosion) and quantified by Euler's number.[8,9] Two processing steps are described in the following.

1. **Feature extraction** - The backprojection images are rendered with continuous response levels, in which both background and defect signals are involved. In order to extract the characteristic shape of a backprojection image, the image is first transformed into a binary image based on a threshold value n_{thv}. Two morphological operations, erosion and dilation, are subsequently applied to the binary image to obtain a feature-extracted version of the original backprojection image. These morphological operations are defined by

$$\epsilon_K(I) = \{\bar{r} | K_r \subset I(x,y)\} \tag{5}$$

$$\delta_V(I) = \{\bar{r} | V_r \cap I(x,y) \neq \emptyset\} \tag{6}$$

where $I(x,y)$ is the backprojection image, ϵ_K is the erosion operator with the erosion structure K, K_r is the eroded set centered at position $\bar{r}$, δ_V is the dilation operator with the dilation structure V, V_r is the dilated set centered at $\bar{r}$, and $\emptyset$ is the empty set. An eight-node element is adopted for both erosion and dilation structures, as shown in Figure 2. The feature extraction operation on $I(x,y)$ is performed on the

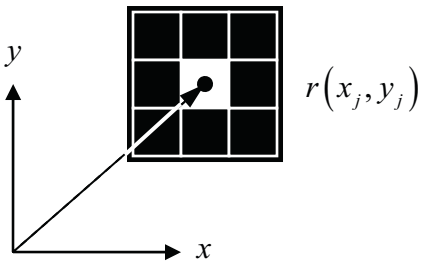

Figure 2. An eight-node element for morphological operations

binary version of $I(x,y)$ in this research, denoted by $I_{BW}(x,y|n_{thv})$. The operation is defined by

$$\hat{I}(x,y|n_{thv}) = \delta_V[\epsilon_K[I_{BW}(x,y|n_{thv})]] \tag{7}$$

where $\hat{I}(x, y|n_{thv})$ is the feature-extracted binary image characterized by a threshold value n_{thv} related to the level of the extracted edge in the image.

2. **Feature quantification** - A quantitative index used in this paper to globally characterize $\hat{I}(x, y|n_{thv})$ is Euler's number, n_E, defined as the number of objects minus the number of holes in an image.

$$n_E(\theta|n_{thv}) = n_{obj}(\theta|n_{thv}) - n_{hol}(\theta|n_{thv}) \tag{8}$$

where $n_{obj}(\theta|n_{thv})$ is the number of objects in $\hat{I}(x, y|n_{thv})$, and $n_{hol}(\theta|n_{thv})$ is the number of holes within the objects in $\hat{I}(x, y|n_{thv})$. With a fixed value of n_{thv}, $n_E(\theta)$ can be obtained.

The presence of damages introduces additional defect signals into backprojection images globally, and changes the maximum amplitude locally. Logically, the presence of scatterers (defect or background) leads to an increasing n_{obj}. The value of $n_E\theta$ is subsequently altered. Given same n_{thv} and same inspection domain Ω_s, the fluctuation of defect scattering signals will create more holes than objects, thus, resulting in small $n_E(\theta)$. The purpose of using mathematical morphology is to quantify such change. Additionally, in view of the angular sensitivity of defect signals, it is believed that damage assessment based on single measurement (or image) is unlikely conclusive. Multiple images (more information) are needed to confirm the speculation on one suspicious image. For this reason, an averaging (low-pass) filter is applied to the $n_E(\theta)$ curve, which is defined by

$$n_E^f(\theta) = \sum_{\theta=-\theta_{int}/2}^{\theta_{int}/2} \frac{n_E(\theta)}{L} \tag{9}$$

where $n_E^f(\theta)$ is the filtered $n_E(\theta)$ curve, and L is the length of the filter. The purpose of this filter is to remove local fluctuations from the original $n_E(\theta)$ curve in order to (i) avoid false alarm at local level and (ii) obtain a globally consistent result. Additionally, the length of the filter suggests the required amount of angular measurements. The length of the filter also relies on the resolution of the image. For high resolution images, small L is expected.

2.3 Optimization

With the use of Euler's number to quantify the backprojection images, optimal parameters can be determined when the differential Euler's number evaluated from the images with and without damages achieves its maximum.

$$\Omega_{opt} = \max_{n_E \in \boldsymbol{Z}} [\Delta n_E(B_{opt}, \theta_{opt})] \tag{10}$$

where B_{opt} denotes the optimal frequency bandwidth, θ_{opt} is the optimal incident angle. $\Delta n_E = n_{E|dam} - n_{E|int}$, $n_{E|dam}$ and $n_{E|int}$ are the n_E of damaged and intact structures, respectively.

3. APPLICATION

3.1 Specimen Description and Laboratory ISAR Measurements

ISAR measurements collected from an artificially-damaged GFRP-wrapped concrete cylinder were collected at the MIT Lincoln Laboratory (LL) for validating the feasibility of FAR NDT. Portland Type I cement was used, and the mix ratio of concrete was water:cement:sand:aggregate = 0.45:1:2.52:3.21 (by weight). The diameter of concrete core was 15.24 cm (6 in), and the heights were 30.4 cm (12 in). The concrete core was cast and cured for 14 days, in which an cubic-like artificial defect (made of Styrofoam) was simultaneously attached on the surface of the concrete form. The artificial defect was a cubic-like Styrofoam (3.81cm-by-3.81cm-by-2.54cm). After the concrete core was cured, a unidirectional glass fabric system (TyfoR SEH-51A by Fyfe Co. LLC) was molded with epoxy resin (TyfoR S Epoxy) to form the GFRP-epoxy sheet wrapped on the surface of the concrete core. The volumetric ratio of epoxy:GFRP was 0.645:0.355. The thickness of the GFRP-epoxy sheet was 0.25 cm (0.1 in). Single layer configuration scheme was adopted.

Radar measurements of the GFRP-confined concrete specimens were conducted at the MIT (Massachusetts Institute of Technology) Lincoln Laboratory using the Compact RCS/Antenna Range facility. Plane wave condition was met when incident waves impinge the specimen. Details of the radar facility were previously reported.[?] Coherent, wide-bandwidth harmonic radar signals linearly HH (transverse electric or TE) polarized at the frequency range of 8 GHz to 12 GHz (X-band) are used in this paper. Figure 3(a) shows the geometry of the specimen. Figures 3(b) and 3(c) show two ISAR measurement sets simulating intact and damaged structures. ISAR measurements of the intact and damage sides of the specimen are provided in Figure 4.

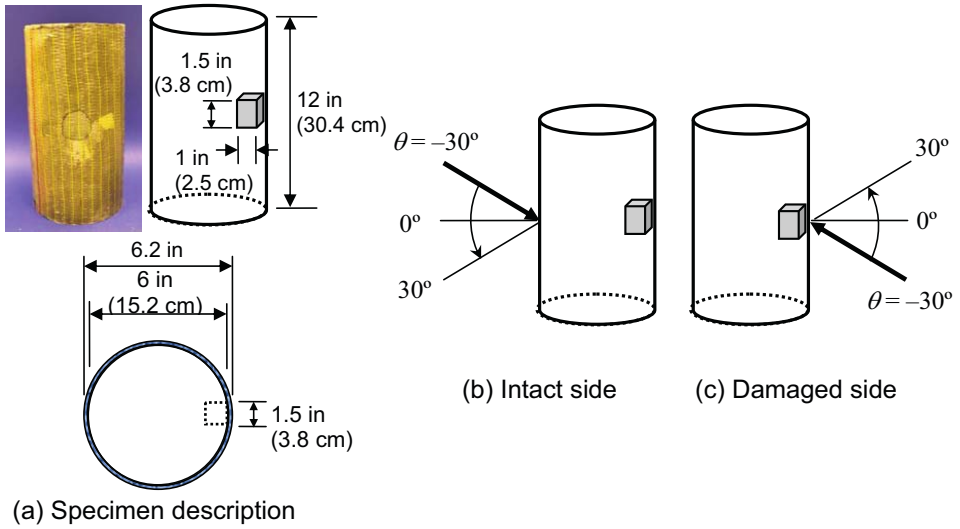

Figure 3. Description of the GFRP-concrete cylinder specimen and its ISAR measurement schemes

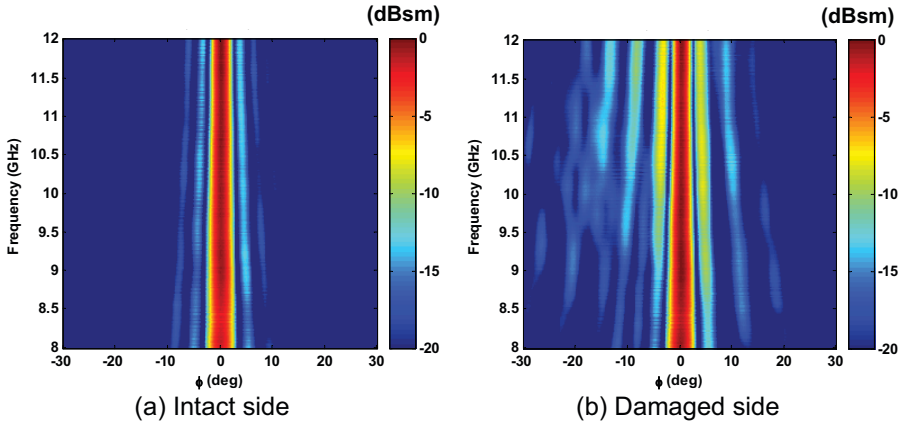

Figure 4. ISAR measurements of the intact and damaged sides of the specimen

3.2 Image Reconstruction and Morphological Processing

The ISAR measurements shown in Figure 4 were processed to render their backprojection images illustrated in Figure 5. In Figure 5, relative position of the specimen is indicated by a solid-line rectangle in each image. In addition to the scatterers due to the edge effect (finite size) from the specimen, it is found that a strong scatter centered at the actual defect location has been successfully reconstructed in the damaged-side backprojection images. Figure 5(b) provides the projection images at $\theta_{int} = 30°, 20°$ and $10°$. In Figure 6 (a), $n_E = -1$, while $n_E = -2$ in Figure 6.

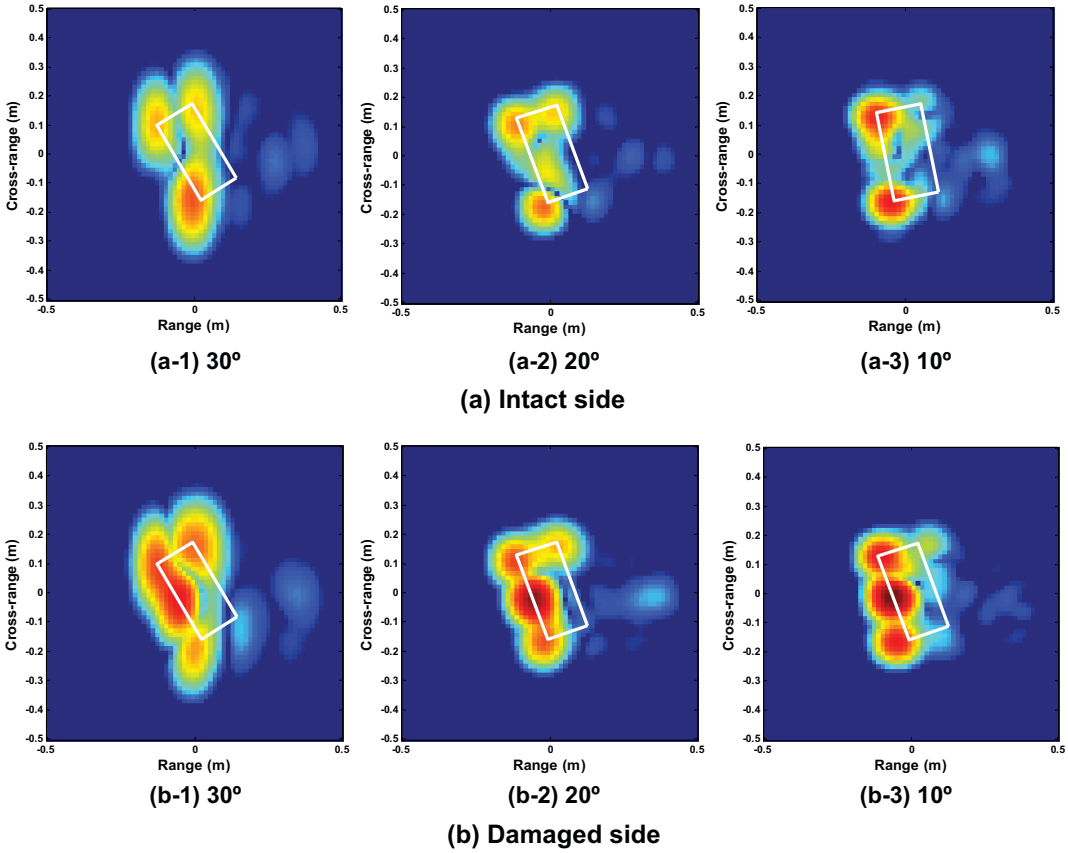

Figure 5. Backprojection images of the intact and damaged sides of the specimen

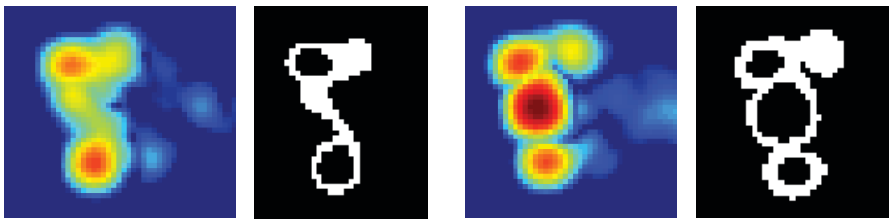

(a) Intact side images – n_{thv} = 0.81 (b) Damaged side images – n_{thv} = 0.73

Figure 6. Morphologically processed images of the intact and damaged sides of the specimen

3.3 Optimal Parameters

To determine the optimal incident angle θ_{opt}, Euler's number n_E for the backprojection images of both the intact and damaged sides of the specimen was calculated. The raw n_E curves respectively representing intact and damaged responses are provided in Figure 7. In Figure 7, it is observed that the n_E values of damaged response fluctuate within the angular range of inspection, while they are in general lower than the n_E values of intact response. The fluctuation of n_E curves is attributed to the variation of ISAR measurements with respect to different incident angles (Figure 4), suggesting that conclusive evaluation should not be made based on single measurement when the image-based technique is applied. It is noteworthy to point out that the specular effect becomes dominant approximately in the angular range of $[-8°, 8°]$; direct evaluation is not possible in the specular-dominant range due to the low signal-to-noise ratio in such range.

To obtain consistent evaluation results, a low-pass filter is applied on the n_E curves in Figure 7. The filtered n_E curves are illustrated in Figure 8. In Figure 8, it is found that the n_E curves are clearly separated after applying a three-point filter; the criterion is to separate the n_E curves outside the specular-dominant range. In this case, the minimum image amount to achieve a consistent evaluation is three. The optimal incident angles in

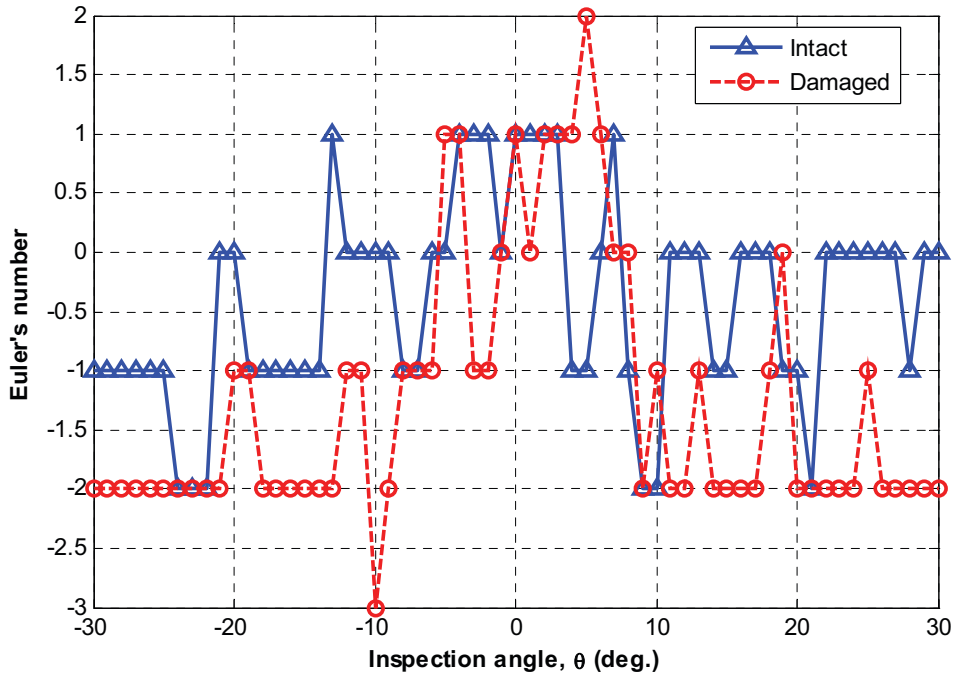

Figure 7. Raw n_E curves representing the intact and damaged responses of the specimen

the angular ranges $[-20°, -8°]$ and $[8°, 20°]$ are $-11°$ and $15°$, respectively; perfect symmetry is not achieved due to the inherent imperfectness (e.g., material heterogeneity and geometric imperfectness) in making the specimen a perfect, symmetric cylinder.

The determination of optimal bandwidth, B_{opt}, is proceeded by comparing the performance of intact and damaged n_E curves using different bandwidths. While it is clear that the greater B the better resolutions (range and cross-range), it is of interest to know the level of reduced bandwidth, at which the differential performance of n_E curves can be identified. Figure 9 (a) provides the relationship between frequency bandwidth (denoted by bandwidth ratio) and the n_E curves of intact and damaged responses. It is found that, in the case of $B = 4$ GHz and $\omega_c = 10$ GHz, the intact and damage n_E curves begin to separate when the chosen bandwidth is greater than $0.6B$. Considering the bandwidth increment to be $0.1B$, the optimal bandwidth B_{opt} is $0.7B$ in this example. This bandwidth (0.7B = 2.8 GHz) also corresponds to a range resolution of 5.31 cm (2 in) and a cross-range resolution of 5.36 cm (2.11 in), as shown in Figure 9 (b). Obviously, with the increase of used bandwidth, damage detectability is improved, as well as image resolutions.

4. SUMMARY AND DISCUSSION

In this paper, a morphological approach is proposed to quantitatively evaluate the difference between backprojection images representing the intact and damaged sides of a GFRP-concrete specimen. Euler's number n_E is applied as the quantitative index. Optimal incident angle and bandwidth are determined by achieving maximum differential n_E. It is found that the presence of an artificial defect embedded at the interface between GFRP sheet and the concrete core can be qualitatively revealed (Figure 5) and quantitatively assessed (Figure 8). Several issues in this paper are also discussed in the following.

- In determining the length of the low-pass filter, the goal is to distinguish the damaged response ($n_E|_{dam}$ curve) from the intact response ($n_E|_{int}$ curve). It should be noted that, from the pattern shown in Figure 4, the presence of defects could be more sensitive to some data points (incident angles) than to the others; the application of a low-pass filter might reduce the contribution from effective data points.

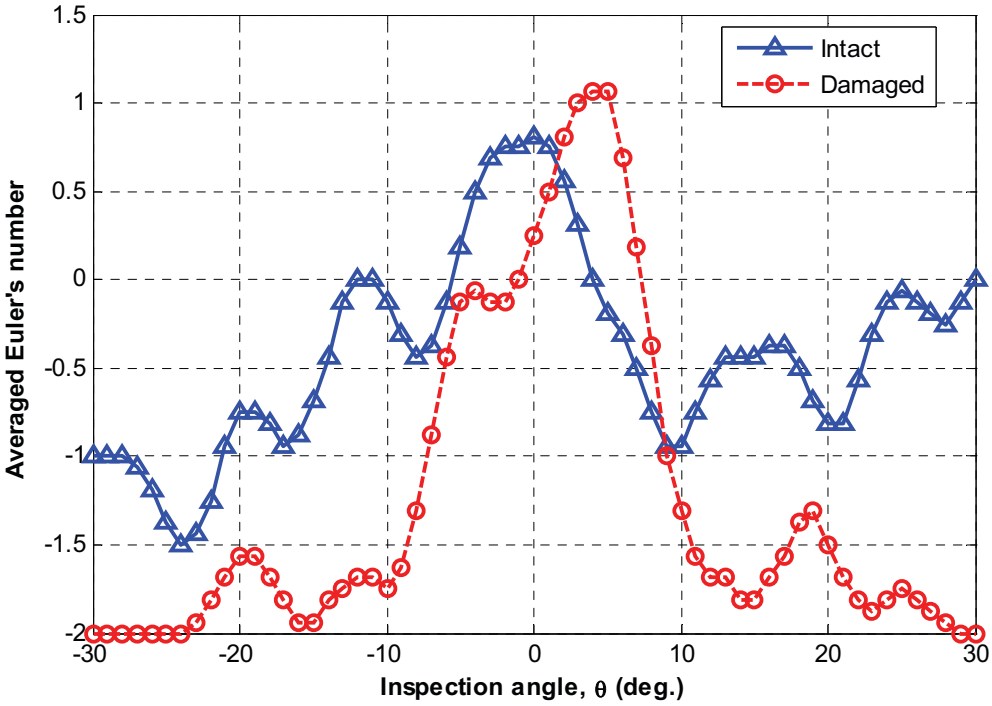

Figure 8. Filtered n_E curves representing the intact and damaged responses of the specimen

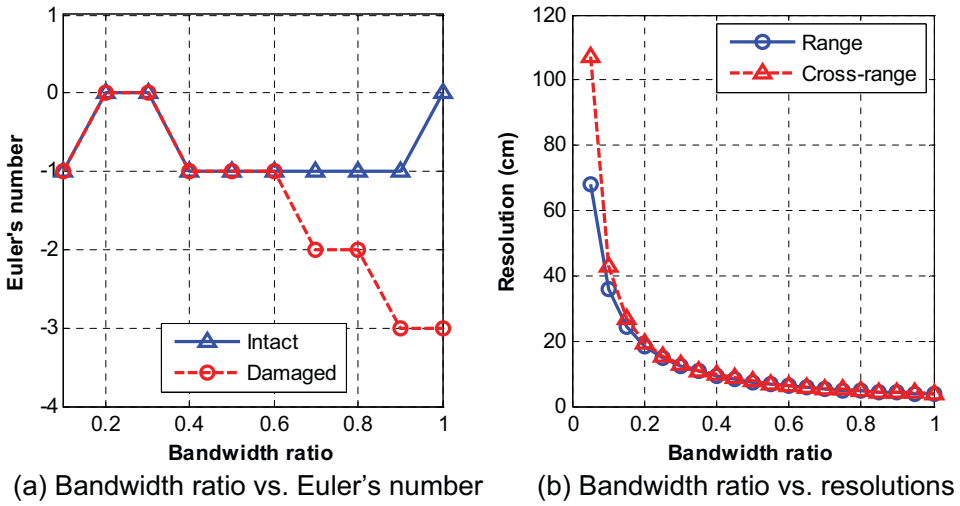

(a) Bandwidth ratio vs. Euler's number (b) Bandwidth ratio vs. resolutions

Figure 9. Intact and damaged n_E values with different bandwidths

- It is expected that the change of defect geometry leads to the change of scattering pattern. Therefore, the determined optimal parameters (frequency bandwidth B and incident angle θ) are associated with the artificial defect used in the example presented in this paper. Nonetheless, the proposed procedure for quantitatively determining optimal parameters is believed applicable for other types of defects and damages.

Ongoing future work include the discrete processing of ISAR measurements (Figure 4) to form the backprojection images with maximum signal-to-noise ratio, and the use of sophisticated morphological structures to improve

the resolution of morphologically-processed images.

5. ACKNOWLEDGMENTS

This work was partially supported by the National Science Foundation through Grant CMS-0324607. The author wants to express his gratitude to the late Professor Jin Au Kong at MIT for the encouragements and supports the author received when conducting the research. The author also thanks D. Bjeler at the MIT Lincoln Laboratory (LL), who supervised the wide-bandwidth radar measurements conducted at the MIT LL.

REFERENCES

1. T.-Y. Yu and O. Buyukozturk, "*A distant real-time radar NDE technique for the in-depth inspection of glass fiber reinforced polymer-retrofitted concrete columns*," *Proc. SPIE* **6934**, San Diego, California, 2008.
2. T.-Y. Yu and O. Buyukozturk, "*A far-field radar NDT technique for detecting debonding in GFRP-retrofitted concrete structures*," *NDT&E Intl.* **4**, pp. 10-24, 2008.
3. L. Tsang, J.A. Kong, and K.-H. Ding, *Scattering of Electromagnetic Waves – Theories and Applications*, John Wiley & Sons, New York, 2000.
4. M. Soumekh, *Synthetic Aperture Radar Signal Processing with MATLAB Algorithms*, Wiley, New York, 1999.
5. J. McCorkle and M. Rofheart, "*An order of $n^2 log n$ backprojection algorithm for focusing wide-angle wide-bandwidth arbitrary-motion synthetic aperture radar*," *Proc. SPIE* **2747**, pp. 25-36, 1998.
6. S. Nilsson and L.-E. Andersson, "*Application of fast backprojection techniques for some inverse problems of synthetic aperture radar*", *Proc. SPIE* **3370**, pp. 62-72, 1998.
7. A.F. Yegulalp, "*Fast backprojection algorithm for synthetic aperture radar*", *Proc. IEEE Radar Conf.*, pp. 60-65, 1999.
8. Y. Shirai, *Three-Dimensional Computer Vision*, Springer-Verlag, Berlin, Germany, 1987.
9. M. Nixon and A. Aguado, *Feature Extraction and Image Processing*, Newnes, Oxford, UK, 2002.